LOGO

CConnect: Synergistic Convolutional Regularization for Cartesian T_2^* Mapping

Juan Molina, Alexandre Bousse, Tabita Catalán, Zhihan Wang, Mircea Petrache, Francisco Sahli, Claudia Prieto and Matías Courdurier

Abstract—**Magnetic resonance imaging (MRI) is fundamental for the assessment of many diseases, due to its excellent tissue contrast characterization. This is based on quantitative techniques, such as T_1, T_2, and T_2^* mapping. Quantitative MRI requires the acquisition of several contrast-weighed images followed by a fitting to an exponential model or dictionary matching, which results in undesirably long acquisition times. Undersampling reconstruction techniques are commonly employed to speed up the scan, with the drawback of introducing aliasing artifacts. However, most undersampling reconstruction techniques require long computational times or do not exploit redundancies across the different contrast-weighted images. This study introduces a new regularization technique to overcome aliasing artifacts, namely CConnect, which uses an innovative regularization term that leverages several trained convolutional neural networks (CNNs) to connect and exploit information across image contrasts in a latent space. We validate our method using in-vivo T_2^* mapping of the brain, with retrospective undersampling factors of 4, 5 and 6, demonstrating its effectiveness in improving reconstruction in comparison to state-of-the-art techniques. Comparisons against joint total variation, nuclear low rank and a deep learning (DL) de-aliasing post-processing method, with respect to structural similarity index measure (SSIM) and peak signal-to-noise ratio (PSNR) metrics are presented.**

Index Terms—**MRI undersampled reconstruction, Machine learning, Quantitative MRI, Iterative reconstruction, T_2^* mapping**

Juan Molina and Matias Courdurier are with the Department of Mathematics, Pontificia Universidad Católica de Chile, Santiago, Chile, and with the Millennium Nucleus for Applied Control and Inverse Problems, Santiago, Chile.

Alexandre Bousse and Zhihan Wang are with the Univ. Brest, LaTIM, Inserm, U1101, 29238 Brest, France.

Tabita Catalán is with the Millennium Nucleus for Applied Control and Inverse Problems, Santiago, Chile, and with the Millennium Institute for Intelligent Healthcare Engineering, Santiago, Chile.

Mircea Petrache is with the Department of Mathematics, Pontificia Universidad Católica de Chile, Santiago, Chile.

Francisco Sahli and Claudia Prieto are with the School of Engineering, Pontificia Universidad Católica de Chile, Santiago, Chile, with the Millennium Institute for Intelligent Healthcare Engineering, Santiago, Chile and the Millennium Nucleus for Applied Control and Inverse Problems, Santiago, Chile.

Corresponding author: Juan Molina, `jjmolina@mat.uc.cl`

I. INTRODUCTION

Quantitative magnetic resonance imaging (MRI) has emerged in recent years as an important non-invasive tool to evaluate a range of neurological conditions, showing great potential for objective characterization of different tissue properties. [1], [2].

Quantitative MRI (qMRI) involves extracting measurable properties to assess the tissue and organs of interest. This includes for example T_1, T_2 and T_2^* mappings [3]. Several clinical studies have shown the potential of T_1 mapping to characterize multiple sclerosis lesions or tumors [4], [5]. T_2 maps have been shown to be valuable in the brain detecting abnormalities in focal epilepsy and cognitive decline [6], [7]. Whereas T_2^* mapping is influenced by iron and myelin content and has been shown to be relevant in characterizing stroke and investigating neurodegenerative diseases, among others [8]–[10].

Conventionally, qMRI parametric mapping requires the acquisition of several three-dimensional (3-D) high-resolution contrast-weighed images followed by a fitting to an exponential model or dictionary matching to generate the corresponding map. Consequently, acquiring qMRI data demands a considerable amount of acquisition time. In order to mitigate this challenge, a common approach is to acquire undersampled measurements [11]. Reconstructing the weighted-contrast images from undersampled data is an ill-posed inverse problem, and regularized undersampling reconstruction techniques are needed to minimize aliasing artifacts [12].

Several iterative regularized reconstruction techniques have been proposed to speed up MRI acquisition [13], [14]. These methods involve iteratively minimizing a functional composed of two components: the data fidelity term, which measures the discrepancy between predictions and acquired data, and the regularization (or penalty) term, which incorporates prior information about the solution. Typically, the fidelity term employs a squared error, while the regularization term has seen numerous innovations over time [14], [15]. Initial regularization efforts emphasized imposing sparsity of the solution using a sparsifying transform combined with a sparsity-promoting norm, such as total variation (TV) and l_1-wavelet regularization [16]–[18]. However, these initial methodologies tended to overlook the redundancies between contrast-weighted images, which is especially relevant in parametric mapping techniques.

A second category of regularization techniques aims at

promoting structural similarity between the image contrasts. Examples in this category include joint total variation (JTV) [19] and nuclear low-rank (NLR) [14], [15]. JTV promotes similar contours between the contrasts, while NLR is designed to exploit redundant local information across contrasts. Despite their effectiveness, the JTV and NLR regularizations are custom-built, they do not always reflect the inherent characteristics of organ-specific anatomic images and may over-regularize pathology signals. Hence, there is still a need to improve MRI image reconstruction techniques to reduce the scanning time and enhance the overall quality of the reconstructed images [20], [21].

Recent years have been marked by the emergence of machine learning (ML) approaches to solve inverse problems [22]–[24]. In image reconstruction, non-deep ML include dictionary learning (DiL), which has been used in MRI [25], [26] as well as in computerized tomography (CT) [27]. More recently, deep learning (DL) techniques have been widely investigated in medical image reconstruction in CT, positron emission tomography (PET) and MRI [28]–[30]. Such approaches include, for example, (i) unrolling architectures, which consist of mimicking an iterative reconstruction algorithm with a DL architecture [31], (ii) direct reconstruction architectures (i.e., raw data to image) [32], [33] and (iii) penalized iterative reconstruction with penalties learned via DL architectures [24], [34]–[36].

Most of the above-mentioned techniques are limited to single-contrast reconstruction. They could benefit to be extended to multicontrast reconstruction in order to take advantage of the information shared across different weighted-contrast images, which is the case in multiparametric mapping. In this paper, we introduce an innovative iterative reconstruction framework that takes advantage of multiple trained convolutional neural networks (CNNs) for a penalized iterative reconstruction with a learned penalty. The proposed approach is investigated in T_2^* mapping of the brain with retrospective undersampled Cartesian acquisition. Inspired from [37], our novel synergistic regularization term leverages redundant information across various image contrasts by the mean of a collection of image-to-image CNNs which connect each contrast to a reference image. Besides, our CNNs are specifically designed and trained to systematically eliminate aliasing artifacts induced by the Cartesian undersampling. This approach, namely ColorConnect, seeks to enhance the quality and fidelity of the reconstructed qMRI images.

The paper is structured as follows: Section II addresses the inverse problem associated with undersampled multi-contrast image reconstruction. Section III describes how to obtain the T_2^* map from the multi-contrast images and offers a concise review of the state-of-the-art of iterative reconstruction techniques for multi-contrast reconstruction. It also outlines classic methods and standard ML techniques, and presents our proposed approach as well as discussing potential alternatives. Section IV introduces in-vivo experiments, presenting results for T_2^* weighted-contrast images and the corresponging T_2^* map, in comparison to state-of-the-art reconstruction methods. Finally, Section V discusses our results and the limitations of the proposed approach, while Section VI summarizes the

conclusion.

II. UNDERSAMPLED MULTI-CONTRAST PROBLEM FORMULATION

In this work, we consider two-dimensional (2-D) images although it can be extended to 3-D volumes without major changes.

A. Forward magnetic resonance (MR) model

The MR signal at time $t > 0$ and spatial frequency $\vec{k}$ is given by the function S defined as [13], [38]

$$S\left(t, \vec{k}\right) = \int c(\vec{r}) M(\vec{r}, t) e^{-2\iota\pi\vec{k}\cdot\vec{r}} \, d\vec{r} \tag{1}$$

$$= \mathcal{F}[c(\cdot)M(\cdot, t)](\vec{k}) \tag{2}$$

where $M(\vec{r}, t)$ is the magnetization at location $\vec{r} \in \mathbb{R}^2$ and time t, c is the coil sensitivity, $\iota = \sqrt{-1}$ and $\mathcal{F}$ denotes the 2-D spatial Fourier transform.

For T_2^* map, the magnetization is assumed to be given by

$$M(\vec{r}, t) = M_0(\vec{r}) e^{-\iota\gamma B_0(\vec{r})t} e^{-t/T_2^*(\vec{r})} \tag{3}$$

where B_0 represents the static magnetic field, M_0 is the initial net magnetization, T_2^* is the transversal relaxation map and γ is a constant (approximately 42.58 MHz/T for hydrogen). For simplicity, we assume a single coil acquisition, i.e., c is constant and equal to one.

Let $\mathcal{K} = \{\mathbf{k}_l\}_{l=1}^N \subset \mathbb{R}^2$ be a finite uniform rectangular grid in the k-space, with N nodes. In the following, given a mapping $g : \mathbb{R}^2 \to \mathbb{C}$, $g(\mathbf{k}) \in \mathbb{C}^N$ denotes the N-dimensional vector defined at each node $l \in \{1, \ldots, N\}$ as $[g(\mathbf{k})]_l = g(\mathbf{k}_l)$.

Let t_i be the acquisition time corresponding to the ith time frame, with $i = 1, \ldots, n_t$. For each i, let $U_i \subset \{1, \ldots, N\}$, $|U_i| = N_i \leq N$, be a subset of indices such that $\{\mathbf{k}_l\}_{l \in U_i}$ is the subset of $\mathcal{K}$ used to sample the acquisition during frame i.

For each i define $\mathcal{P}_i : \mathbb{C}^N \to \mathbb{C}^{N_i}$ the subsampling operator given by

$$\mathcal{P}_i(\{z_l\}_{l=1}^N) = \{z_l\}_{l \in U_i}, \quad \forall \{z_l\}_{l=1}^N \in \mathbb{C}^N. \tag{4}$$

Let $Y_i \in \mathbb{C}^{N_i}$ represent the ith measurement in the k-space. Following the forward model introduced above in this section (with $c = 1$), we have

$$\begin{aligned} Y_i &= \mathcal{P}_i\left(S\left(t_i, \mathbf{k}\right)\right) + \epsilon_i \\ &= \mathcal{P}_i\left(\mathcal{F}[M(\cdot, t_i)](\mathbf{k})\right) + \epsilon_i \end{aligned} \tag{5}$$

where $\epsilon_i \in \mathbb{C}^{N_i}$ is a zero-mean measurement noise.

B. Inverse problem

The inverse problem is first formulated as

$$\begin{aligned} &\text{find} \quad M(\cdot, t_i) \quad \text{s.t.} \\ &Y_i \approx \mathcal{P}_i\left(\mathcal{F}\left[M(\cdot, t_i)\right](\mathbf{k})\right) \quad \forall i \end{aligned} \tag{6}$$

Equation (6) is a semi-discrete inverse problem and needs to be fully discretized for numerical experiments.
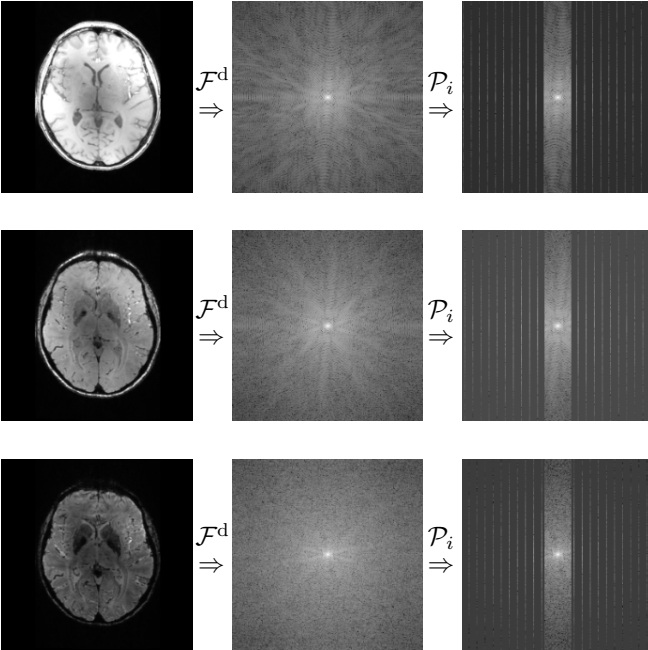
Assume $M(\cdot, t)$ lies in a finite-dimensional space defined by N pixels such that

$$M(\vec{r}, t) = \sum_{j=1}^{N} x_j(t) m_j(\vec{r}) \qquad (7)$$

where each $m_j \colon \mathbb{R}^2 \to \mathbb{R}$ is a function spatially describing the jth pixel center at position $r_j \in \mathbb{R}^2$ (we require that $m_j(r_i) = \delta_{ij}$, the Kronecker delta) and $x_j(t) \in \mathbb{C}$ is the linear factor of pixel j at time t. Substituting (7) in (5) and using the linearity of the operators, we have

$$\mathcal{P}_i\left(\mathcal{F}[M(\cdot, t_i)](\mathbf{k})\right) = \sum_{j=1}^{N} \mathcal{P}_i\left(\mathcal{F}[m_j](\mathbf{k})\right) x_j(t_i)$$
$$= \mathcal{A}_i X_i \qquad (8)$$

where $X_i = (x_1(t_i), \ldots, x_N(t_i))^T \in \mathbb{R}^N$, and $\mathcal{A}_i = \mathcal{P}_i \mathcal{F}^{\mathrm{d}}$ with $\mathcal{F}^{\mathrm{d}} \in \mathbb{C}^{N \times N}$ defined as $\left[\mathcal{F}^{\mathrm{d}}\right]_{l,j} = \mathcal{F}[m_j](\mathbf{k}_l)$, is a discrete Fourier-like transformation. The operator $\mathcal{A}_i = \mathcal{P}_i \mathcal{F}^{\mathrm{d}}$ is illustrated in Figure 1.

Fig. 1: Illustration of the forward operator $\mathcal{A}_i = \mathcal{P}_i \mathcal{F}^{\mathrm{d}}$ applied to three different X_i. The k-space images are represented by their complex magnitude.

The continuous-to-discrete forward model (5) becomes discrete, i.e.,

$$Y_i = \mathcal{A}_i X_i + \epsilon_i, \qquad (9)$$

and the corresponding discrete inverse problem is:

$$\text{find} \quad X_i \in \mathbb{R}^N \quad \text{s.t.}$$
$$Y_i \approx \mathcal{A}_i X_i \quad \forall i. \qquad (10)$$

In this paper, each measurement Y_i is obtained with Cartesian undersampling. As mentioned above, undersampling is a common practice as it reduces scanning time. However, it also reduces the amount of measurements available, resulting in the non-uniqueness of the solution to the inverse problem and provoking aliasing artifacts [11].

III. PROPOSED METHOD

The reconstruction of T_2^*-mapping is usually carried out by undertaking two tasks.

The first step is to reconstruct the multicontrast image $\{X_i\} = \{X_i, i = 1, \ldots, n_{\mathrm{t}}\}$ by iterative reconstruction, i.e., by iteratively minimizing a functional of the form

$$\min_{\{X_i\}} \sum_{i=1}^{n_{\mathrm{t}}} \mathcal{L}_i(X_i) + \beta \mathcal{R}\left(X_1, \ldots, X_{n_{\mathrm{t}}}\right) \qquad (11)$$

where $\mathcal{L}_i$ represents the data fidelity term quantifying the disparity between the reconstruction X_i and the measurement Y_i through the forward operator $\mathcal{A}_i$, typically

$$\mathcal{L}_i(X_i) = \frac{1}{2}\left\|\mathcal{A}_i X_i - Y_i\right\|_2^2 \qquad (12)$$

where $\|\cdot\|_2$ denotes the ℓ^2-norm. $\mathcal{R}$ denotes a regularization term that imposes individual and/or joint properties on the images, and $\beta > 0$ is the penalty parameter. The main contribution of this paper is the improvement of this first step through the design of $\mathcal{R}$.

The second step corresponds to estimating $T_2^*(\vec{r})$ at each pixel r_j, with $j = 1, \ldots, N$, by curve fitting using the magnitude of a discrete version of (3) evaluated at $t = t_i$, $i = 1, \ldots, n_{\mathrm{t}}$ (see [39]). Namely, considering the discrete representations

$$T_2^*(\vec{r}) = \sum_{j=1}^{N} \tau_j m_j(\vec{r}) \qquad (13)$$

and

$$\left| M_0(\vec{r}) \mathrm{e}^{-i\gamma B_0(\vec{r})} \right| = \sum_{j=1}^{N} d_j m_j(\vec{r}), \qquad (14)$$

τ_j, d_j are estimated for each $j = 1, \ldots, N$ from equation (3) evaluated at r_j, i.e., by solving

$$|x_j(t_i)| \approx d_j \exp\left(-\frac{t_i}{\tau_j}\right), \quad i = 1, \ldots, n_{\mathrm{t}}. \qquad (15)$$

A. Conventional Methods

Iterative reconstruction methods with different regularization terms have been proposed over the last decades to incorporate prior information in undersampled MRI reconstruction. Two state-of-the-art methods that exploit redundancies across the contrast dimension and JTV and NLR reconstruction.

1) Joint Total Variation: Compressed sensing (CS) techniques, in an *analysis* model, address under-sampling by leveraging the sparsity of the reconstructed images using penalties of the form

$$\mathcal{R}_{\mathrm{CS}}\left(\{X_i\}\right) = \left\|T\left(\{X_i\}\right)\right\|_q \qquad (16)$$

where $T \colon \mathbb{R}^{N \times n_{\mathrm{t}}} \to \mathbb{R}^M$ is a sparsifying transform and $\|\cdot\|_q$ is either the ℓ_1-norm or the ℓ_0 semi-norm. Examples in the literature include TV [40], [41] as well as l_1-wavelet regularization [42], [43]. These approaches could be used to

define the regularization term in (11) by applying the penalty for each contrast independently.

Inter-contrast information can also be exploited to "consolidate" the images, for example with JTV defined as

$$\mathcal{R}_{\text{JTV}}\left(\{X_i\}\right) = \sum_{j=1}^{N} \sqrt{\sum_{i=1}^{n_{\text{t}}} \left\|\left[\nabla X_i\right]_j\right\|_2^2} \tag{17}$$

where $\nabla : \mathbb{R}^N \rightarrow \left(\mathbb{R}^N\right)^2$ denotes the discrete 2-D gradient [19], [44], which promotes joint sparsity of the X_is across contrasts. Other examples include total nuclear variation (TNV) [45] and parallel level-set (PLS) [46]. These works report noise and artifact reduction as compared to reconstructing the contrast images individually.

2) Nuclear Low Rank: NLR method involves controlling the rank of the multicontrast (Casorati) matrix achieved by promoting linear dependencies between contrast [15], [47]. Given the shared structures across different contrasts, assuming a form of low rank in the multicontrast matrix is relevant due to the redundant information between them. The corresponding penalty is defined as

$$\mathcal{R}_{\text{NLR}}(X) = \|X\|_* \tag{18}$$

where $X = [X_1, \ldots, X_{n_{\text{t}}}] \in \mathbb{R}^{N \times n_{\text{t}}}$, $\|\cdot\|_*$ is the nuclear norm defined as the sum of singular values, that is, from the singular value decomposition $X = U \Sigma V^T$, $\|X\|_* = \text{tr}(\Sigma)$.

B. Our Approach: CConnect

Classical regularization methods discussed in subsection III-A, such as NLR and JTV, enforce geometric similarities between contrasts. However, these strictly geometrical assumptions may not universally hold true, as anomalies or organ defects can modify individual patient measurements. Relying solely on prescribed similarity assumptions might fail to capture the variations inherent in patient-specific data accurately. On the contrary, ML and more particularly DL techniques aim at learning image characteristics from a training dataset which can be used as a prior information during image reconstruction. Our approach is derived from Uconnect for multi-energy CT [37], which is inspired from DiL and described in the next subsection.

1) Inspiration: Multicontrast Dictionary Learning: The general idea is to assume that the image can be sparsely decomposed in a basis of trained atoms that form a dictionary. A single decomposition for an entire image is often impractical and therefore it is achieved on a patch basis. In the context of multi-contrast MRI, the corresponding penalty is defined as

$$\mathcal{R}_{\text{DiL}}\left(\{X_i\}\right) = \min_{\{z_p\}} \sum_{i=1}^{n_{\text{t}}} \sum_{p=1}^{n_{\text{p}}} \frac{1}{2}\|P_p X_i - D_i z_p\|_2^2 + \alpha\|z_p\|_q \tag{19}$$

where $P_p \in \mathbb{R}^{d \times N}$ is the p-th patch extractor, $p = 1, \ldots, n_{\text{p}}$ $D_i \in \mathbb{R}^{d \times S}$ is the dictionary that corresponds to the ith contrast, and each $z_p \in \mathbb{R}^S$ is the sparse code for each patch p. $\|\cdot\|_q$ (ℓ^0 of ℓ^1), and $\alpha > 0$. DiL is a *synthesis* model for CS. Note that in this formulation a single sparse z_p code is

used such that the information is conveyed across the contrasts $i = 1, \ldots, n_{\text{t}}$. This constraint can be relaxed by utilizing one sparse code per image with a joint sparsity norm [48].

Unsupervised training of the dictionaries involves minimizing the expression (19) across a training dataset containing multicontrast images. However, accurately representing all potential contrast images demands a substantial number of atoms, leading to a high computational cost during training. Additionally, the inefficiency of patch-based DiL may arise from the shift-variant nature of atoms, resulting in duplicates during the training process. Moreover, employing numerous neighboring or overlapping patches across training images is suboptimal for sparse representation, as sparsification occurs independently on each patch.

2) Proposed Approach: Our method, namely CConnect, proposes an alternative to multicontrast DiL that does not require a patch decomposition and, more importantly, that is easier to train. Specifically, our method requires only one mapping, taking the form of an image-to-image CNN, for each contrast.

We define the following penalty that resembles (19),

$$\mathcal{R}_{\text{CC}}(\{X_i\}) = \min_{z \in \mathbb{R}^N} \sum_{k=1}^{n_{\text{t}}} \|f_i(z) - X_i\|_2^2 + \alpha \mathcal{H}(z) \tag{20}$$

where each $f_i : \mathbb{R}^N \rightarrow \mathbb{R}^N$ is a trained CNN that maps a single latent image $z \in \mathbb{R}^N$ to an image in the ith channel and $\mathcal{H}$ is a regularization term for z (with weight $\alpha > 0$). $\mathcal{R}_{\text{CC}}$ is minimized if the X_is are "connected" through a single z that is "smooth" in the sense of $\mathcal{H}$. In [37], in the context of multi-energy spectral CT reconstruction, z corresponds to a "reference image" corresponding to the lowest-energy image. By connecting all the channels to a reference image, the entire raw data set $\{Y_i\}$ is used for the reconstruction of all channel X_i.

In this work, the latent variable takes the form of a mean image $\overline{X}$,

$$\overline{X} = \frac{1}{n_{\text{t}}} \sum_{i=1}^{n_{\text{t}}} X_i, \tag{21}$$

and the CNNs f_i are trained such that

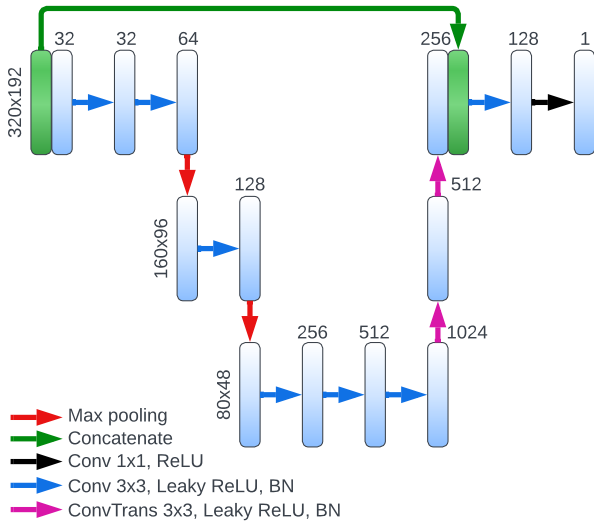$$f_i\left(\overline{X}\right) \approx X_i \quad \forall i = 1, \ldots, N. \tag{22}$$

The choice of z being the mean image is deliberate. Each contrast holds distinct information that is not present in the others, primarily due to the undersampling method employed. Additionally, the first contrasts have more prominent features, making extracting features from them more notorious than the other contrasts.

Finally, we used an ℓ_1-wavelet regularization (WR) penalty $\mathcal{H} = \mathcal{R}_{\text{CS}}$ as in (16) where T was chosen as Haar wavelet transform [49], although other regularizers can be used, for example the Huber penalty as proposed in [37]. In our case, the wavelet regularization has the best result since the referent image z is not necessarily smooth.

3) Architecture and training : We designed CConnect's architecture (i.e., the f_is) as a CNN with an encoder and decoder comprising nine convolutional layers for a total of

215 million parameters, see Figure 2. CConnect architecture resembles the UNet model [50], however the fact that it has a unique skip connection and employs leaky ReLU as activation functions make the model able to address coherent aliasing artifacts created by Cartesian undersampling, which a standard UNet is not capable to correct according to our exploratory experiments.

Fig. 2: CConnect architecture (i.e., the f_is). 'Conv' denotes the discrete convolution, 'ConvTrans' is the inverse operation of the convolution and BN means batch normalization. Additionally, each numerical value in the figure corresponds to the number of features in the output. The max pooling operation reduces the size of the images to half while the ConvTrans operation increases their size by two.

The CNNs f_i, $i = 1, \ldots, n_t$, through the regularization (20), are required (i) to convey information between contrasts by connecting all contrast to a single latent image z and (ii) to remove aliasing artifacts due to undersampling. For this purpose, we will augment the datasets as follows: Let $\left\{ X_{k,i}^\star, i = 1, \ldots, n_t \right\}_{k=1}^K$ be the initial dataset comprising K clean contrast images sequences. For each $k = 1, \ldots, K$ we define the "clean mean image" as

$$\overline{X}_k^\star = \frac{1}{n_t} \sum_{i=1}^{n_t} X_{k,i}^\star. \qquad (23)$$

and the "mean aliased image" as

$$\widehat{X}_k = \frac{1}{n_t} \sum_{i=1}^{n_t} \widehat{X}_{k,i}, \qquad (24)$$

where the contrasts sequence $\{\widehat{X}_{k,i}\}_{i=1}^{n_t}$ are reconstructed images obtained by solving (11) with $\beta = 0$ (using a conjugate gradient (CG) method with stopping criteria being the norm of the gradient being less than 10^{-5}), thus suffering from remaining aliasing due to the undersampling. For each CNN f_i, the training dataset is partitioned as
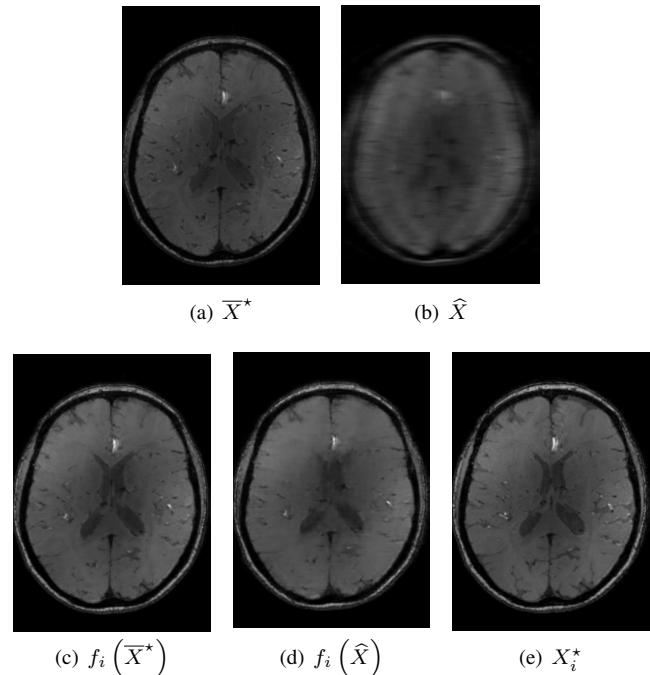
$$\left\{ \left(\overline{X}_k^\star, X_{k,i}^\star \right) \right\}_{k=1}^K \cup \left\{ \left(\widehat{X}_k, X_{k,i}^\star \right) \right\}_{k=1}^K, \qquad (25)$$

and each f_i is trained such that

$$f_i\left(\overline{X}_k^\star \right) \approx X_{k,i}^\star \quad \text{and} \quad f_i\left(\widehat{X}_k \right) \approx X_{k,i}^\star \quad \forall k, i. \qquad (26)$$

The training is achieved by minimizing a mean square error as the loss function using Adam with weight decay regularization and learning rate of 10^{-4} [51]. Each sequence of contrasts, $\{X_{k,i}^\star\}$ and $\{\widehat{X}_{k,i}\}$, in the dataset are normalized by the maximum value of the first clean contrast $X_{k,1}^\star$, $k = 1, \ldots, K$. Additionally, it is crucial to note that the trained functions depended on the specific aliasing present on $\widehat{X}_{k,i}$, which in turn depends entirely on the undersampling pattern. Consequently, it is necessary to train specific CConnect functions for each distinct undersampling pattern.

Figure 3 shows an example of a trained CNN f_i, $i = 3$, mapping a mean clean image $\overline{X}^\star = \frac{1}{n_t} \sum_{i=1}^{n_t} X_i^\star$ and a mean aliased image $\widehat{X} = \frac{1}{n_t} \sum_{i=1}^{n_t} \widehat{X}_i$ to the target image $X^\star$ (all of which were taken from the testing dataset). We observe that the mapped images $f_i\left(\overline{X}^\star \right)$ and $f_i\left(\widehat{X} \right)$ are similar to the target clean image $X_i^\star$, which shows that our trained model can generalize to a testing dataset.

(a) $\overline{X}^\star$ (b) $\widehat{X}$

(c) $f_i\left(\overline{X}^\star \right)$ (d) $f_i\left(\widehat{X} \right)$ (e) $X_i^\star$

Fig. 3: Illustration of a trained mapping f_i ($i = 3$) on an clean averaged image $\overline{X} = \frac{1}{n_t} \sum_{i=1}^{n_t} X_i^\star$ and a mean aliased image $\widehat{X} = \frac{1}{n_t} \sum_{i=1}^{n_t} \widehat{X}_i$.

4) Reconstruction Algorithm: Solving (11) using the synergistic penalty (20) is achieved through alternating minimization with respect to $\{X_i\}$ and z. Given the estimates $\left\{ X_i^{(n)} \right\}$ and $z^{(n)}$ at iteration n, the updated estimates at iteration $n+1$

are computed as follows:

$$X_i^{(n+1)} = \underset{X_i \in \mathbb{R}^N}{\arg\min} \ L_i(X_i) + \beta \frac{1}{2} \left\| m f_i \left(\frac{z^{(n)}}{m} \right) - X_i \right\|_2^2 \ \forall i,$$
(27)

$$z^{(n+1)} \in \underset{z \in \mathbb{R}^N}{\arg\min} \ \sum_{i=1}^{n_t} \frac{1}{2} \left\| m f_i \left(\frac{z}{m} \right) - X_i^{(n)} \right\|_2^2 + \alpha \mathcal{H}(z)$$
(28)

(where m is described below). Each sub-problem is approximately solved using iterative algorithms. We used one iteration of the CG method [52] for (27), and one outer iteration of the alternating direction method of multipliers (ADMM) [53] for each step on (28). The initial images are defined as $X_i^{(0)} = \widehat{X}_i$ where $\widehat{X}_i$ is reconstructed from Y_i by solving (11) with $\beta = 0$ (also with a CG method), while z was initialized as $z^{(0)} = \frac{1}{n_t} \sum_{i=1}^{n_t} \widehat{X}_i$. The stopping criterion is determined when the ℓ^2-norm of the gradient of the sub-problem (27) begins to increase.

The normalization constant m in (27) and (28) is chosen as $m = \max \left(X_1^{(0)} \right)$ and is required since the f_i are trained with normalized sets.

The optimization problem is not convex due to the f_is and therefore proving the convergence is challenging. Nevertheless, we observed in our experiments that the algorithm decreases the objective function at each iteration, and that it behaves as if it converges, for a wide range of β-values.

C. Comparison with other DL Techniques

ML and DL has significantly influenced medical image reconstruction [54]. Several approaches share similarities with our methodology, utilizing DL as a tool to enhance iterative reconstructions [55], [56]. However, a comparison of our proposed approach to other DL techniques presents some challenges. For once, DL models are usually not open-source or demand substantial efforts for replication, involving adjustment to the specific data structure and fine-tuning of the hyperparameters that are heavily dependent on the used dataset. Additionally, we are using a Cartesian undersampling patterns with a structure across contrasts that complement information through them. This hinders comparison with DL techniques developed for other undersampling patterns that would not work well in our case [57].

Alternatively, we could compare to methods that employ DL for image post-processing, such as denoising. But for denoising techniques to achieve good results in MR images reconstructed from undersampled measurements, the undersampling must follow radial or random patterns, since in such cases, artifacts resemble noise [58], while our undersampling pattern generates strong structured aliasing artifacts.

Nonetheless, as part of our validation, we compared our approach with a standard de-aliasing method designed by us. We label this technique de-aliasing (DeAli) and we describe it here. The DeAli method consists in obtaining a aliased initial image $\widehat{X}_i$, reconstructed from each undersampled measure-

ment Y_i as

$$\widehat{X}_i \in \underset{X \in \mathbb{R}^N}{\arg\min} \ \frac{1}{2} \| \mathcal{A}_i X - Y_i \|_2^2$$
(29)

using CG, and then, the DeAli reconstruction, is obtain by applying an image post-processing g_i, $i = 1, \ldots, n_t$, which is a trained image-to-image CNNs such that

$$g_i(\widehat{X}_i) \approx X_i^\star .$$
(30)

Here, the DeAli CNNs g_i share the same design as the CConnect CNNs f_i. The unique difference lies in the definition of the training set, which is given by:

$$\left\{ \left(\widehat{X}_{k,i}, X_{k,i}^\star \right) \right\}_{k=1}^K .$$
(31)

for $i = 1, \ldots, n_t$. Once the g_i are trained, they are used to de-aliase any reconstruction with the same undersampling pattern.

IV. EXPERIMENTS

A. Data Sets and CNN Training

Multi-contrast MR images from the SENIOR cohort [59] were acquired on a 7-Tesla MAGNETOM Terra scanner (Siemens Healthineers, Erlangen, Germany) equipped with a 32-channel head coil, at Biomaps, Service Hospitalier Frédéric Joliot, Orsay, France.
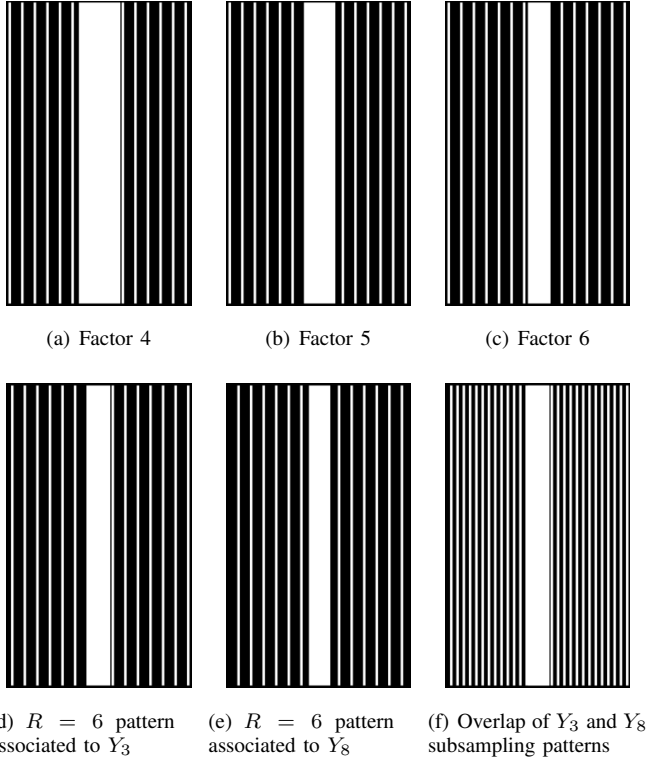
This initial dataset had echo times t_i 1.68, 4.73, 7.78, 10.83, 13.88, 16.93, 19.98, 23.03, 26.08 and 29.13 ms, i.e., 10 contrasts, a repetition time of 37 ms, voxel size of 0.8 mm $\times$0.8 mm$\times$0.8 mm, a 256 mm field-of-view, 740 Hz/Px bandwidth and were reconstructed using GRAPPA [60]. The total acquisition time was 9 minutes and 48 seconds per patient. The complete dataset included five patients, and each of them contained the magnitude of 10 T_2^*-weighted 3-D brain images of dimensions $192 \times 320 \times 320$.

From the initial dataset, we extracted 100 (out of 320) high-quality (i.e., low-noise, aliasing-free) multi-contrast brain 2-D MR images (slices) from each patient. The $K = 300$ multi-contrast images from the first three patients were used to form the CNNs training set. We formed the development set of early stopping criteria in the CNNs training with the multi-contrast images from the 4th patient, while we used the multi-contrast images from the 5th patient to evaluate the proposed reconstruction method.

Each high-quality multi-contrast (real-valued) image $\{X_i^\star, \ i = 1, \ldots, n_t\}$ was used as a ground truth (GT) reference image. To simulate the raw data and retrospective undersampling $\{Y_i, \ i = 1, \ldots, n_t\}$ we used the discrete forward model (9) (with $\epsilon_i = 0$), i.e., the simulated measurement Y_i was obtained by performing the Fourier transform of $X_i^\star$ and then undersampling the result with the sampling operator $\mathcal{P}_i$.

We considered three different undersampling factors, $R = 4$, $R = 5$, and $R = 6$, using a uniform Cartesian trajectory with a fully sampled central region. For $R = 4$ the pattern fully samples 32 readouts in the k-space center and uniformly samples 16 readouts in the outer region of the k-space. Similarly, for $R = 5$ the pattern samples 24 readouts in the

k-space center and 8 readouts in the region of the k-space, whereas for $R = 6$ the pattern samples 16 readouts in the k-space center and uniformly samples 8 readouts in the outer region of the k-space. For a fixed factor R, the undersampling patterns $\mathcal{P}_i$ for different contrasts i are such that they all fully sample the k-space center, but the outer sampled readouts are shifted and do not overlap between contrasts (see Figure 4).
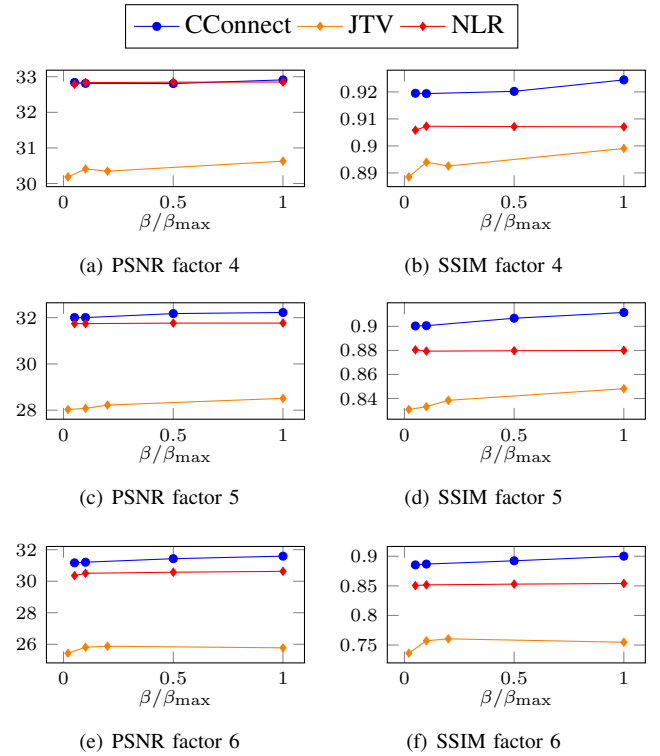

(a) Factor 4   (b) Factor 5   (c) Factor 6

(d) $R = 6$ pattern associated to Y_3 (e) $R = 6$ pattern associated to Y_8 (f) Overlap of Y_3 and Y_8 subsampling patterns

Fig. 4: Illustration of the undersampling pattern for three acceleration factors. The first row shows the undersampling patterns for acceleration factors $R = 4$, $R = 5$ and $R = 6$ associated with measurement Y_1. The second row shows the undersampled pattern for an acceleration factor $R = 6$ for the third and eighth measurements, and their overlap.

Specialized software and high-performance hardware are crucial elements in DL. We used TensorFlow and JAX [61] to implement and train the CNNs, specifically utilizing specialized JAX libraries such as Optax and Flax, for efficient implementation and fine-tuning of the neural networks. In terms of hardware, we used an NVIDIA GeForce GTX 1660 Ti with 6GB memory.

B. Metrics

In order to evaluate the quality of a reconstructed image with respect to a reference image, we used structural similarity index measure (SSIM) and peak signal-to-noise ratio (PSNR) [62]. These metrics are important in evaluating and quantifying image fidelity and perceptual quality. Each metric offers unique insights into different aspects of image quality, ranging from pixel-level differences to human perceptual sensitivity. PSNR tends to focus more

(a) PSNR factor 4   (b) SSIM factor 4

(c) PSNR factor 5   (d) SSIM factor 5

(e) PSNR factor 6   (f) SSIM factor 6

Fig. 5: PSNR and SSIM mean values of the reconstructed T_2^*-weighted images using different values of penalty parameter β for the iterative methods.

on pixel-wise differences and is easier to compute, while SSIM considers structural information and human perception, making it more robust for evaluating perceptual quality. We utilized the functions `structural_similarity` and `peak_signal_noise_ratio` from the Python package `skimage` to compute the PSNR and SSIM.

C. Results

1) T_2^*-weighted Image Reconstruction: Reconstructions results for T_2^*-weighted images using no regularization (naive-solution), DeAli, JTV, NLR and the proposed CConnect method are shown in Figure 6 for $R = 6$ in a representative 2D slice in comparison to the GT. The penalty parameters were fixed for each reconstruction. The values are $\beta = 5 \cdot 10^6$ for NLR, $\beta = 5 \cdot 10^6$ for JTV and finally, $\beta = 10^4$ and $\alpha = 10^6$ for CConnect, which are chosen for each method in their optimal range. Significant remaining aliasing is observed for the No Reg and JTV methods. DeAli and NLR achieved better results, although remaining aliasing is still visible for the 3th contrast in this case. CConnect achieves the best results for both contrasts.

Table I shows the mean and standard deviation of metrics across the reconstruction of T_2^*-weighted images from 50 distinct 2-D slices in the testing dataset, considering undersampling factors of $R = 4$, $R = 5$, and $R = 6$. Notably, CConnect emerges with the most favorable mean values, and the standard deviation exhibits a comparable order of magnitude across the evaluated methods. The computation time for all the methods
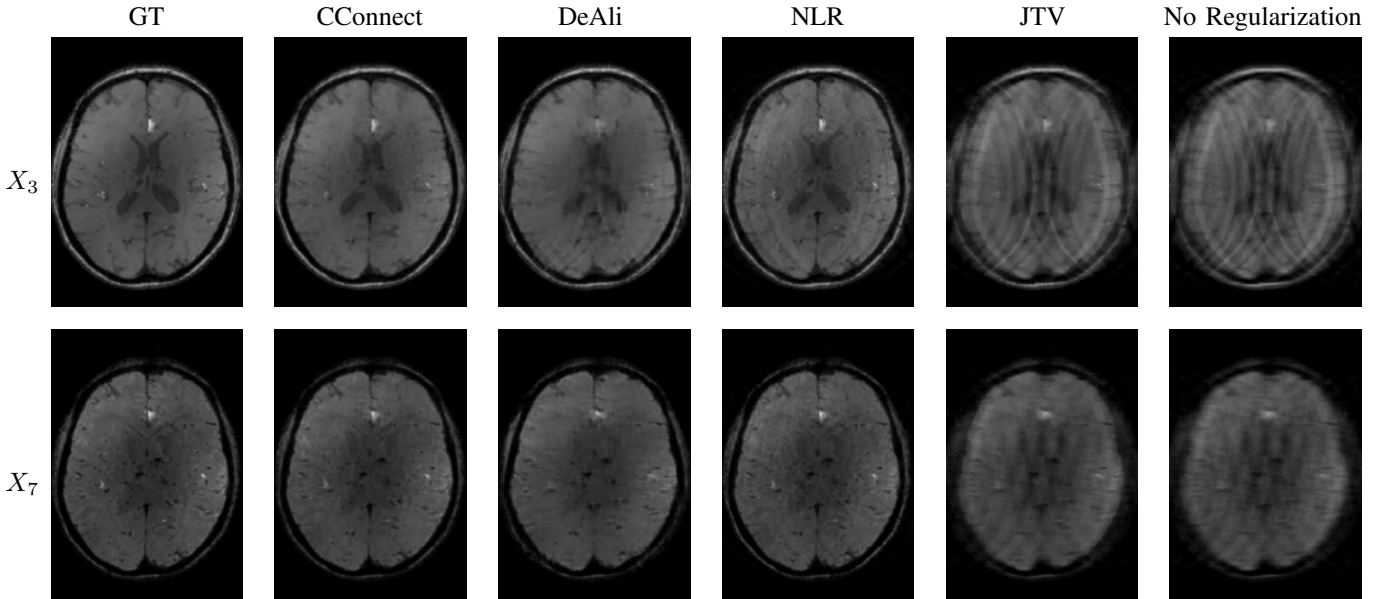
Fig. 6: Reconstruction results for undersampling factor $R = 6$ for slice 70 of the test set. GT, the proposed CConnect, DeAli, NLR, JTV and no regularization are included.

TABLE I: Metrics of the reconstruction of T_2^*-weighted images, average computed for the reconstruction of slides 30 to 79.

	$R = 4$		$R = 5$		$R = 6$	
	PNSR	SSIM	PNSR	SSIM	PNSR	SSIM
DeAli	29.191 ± 1.345	0.869 ± 0.019	26.802 ± 1.28	0.815 ± 0.019	25.06 ± 0.947	0.757 ± 0.021
JTV	30.84 ± 1.281	0.898 ± 0.015	28.283 ± 0.979	0.833 ± 0.021	25.8 ± 0.987	0.749 ± 0.02
NLR	$\mathbf{33.038 \pm 2.195}$	0.905 ± 0.027	31.828 ± 2.176	0.876 ± 0.033	30.722 ± 2.082	0.85 ± 0.035
CConnect	32.834 ± 2.064	$\mathbf{0.922 \pm 0.022}$	$\mathbf{32.108 \pm 2.125}$	$\mathbf{0.907 \pm 0.028}$	$\mathbf{31.55 \pm 2.094}$	$\mathbf{0.895 \pm 0.03}$

TABLE II: Metrics of the reconstruction of T_2^* map, average computed for the reconstruction of slides 30 to 79.

	$R = 4$		$R = 5$		$R = 6$	
	PNSR	SSIM	PNSR	SSIM	PNSR	SSIM
DeAli	28.52 ± 0.95	0.902 ± 0.015	28.896 ± 0.787	0.887 ± 0.021	26.44 ± 0.504	0.849 ± 0.022
JTV	30.507 ± 0.779	0.918 ± 0.009	29.07 ± 0.544	0.883 ± 0.019	27.289 ± 0.45	0.85 ± 0.021
NLR	30.162 ± 0.523	0.912 ± 0.014	29.39 ± 0.542	0.895 ± 0.017	28.995 ± 0.506	0.879 ± 0.017
CConnect	$\mathbf{30.801 \pm 0.576}$	$\mathbf{0.92 \pm 0.011}$	$\mathbf{30.018 \pm 0.802}$	$\mathbf{0.907 \pm 0.016}$	$\mathbf{29.213 \pm 0.729}$	$\mathbf{0.894 \pm 0.017}$

is in the same order of magnitude (a few hours). CConnect is the most time-intensive, taking 2 to 3 times longer than JTV or NLR, and DeAli is the fastest, being a non-iterative method.

Finally, to analyze the methods' robustness concerning the penalty parameter β, we present the evaluation metrics of JTV, NLR, and CConnect methods for different values of β on all factors in the case slice 50 (Figure 5). The range of β is displayed in a relative scale for each method, in order to compare robustness between the different methods. CConnect and NLR exhibit similar PSNR values for different penalty parameters β; nevertheless, our method outperforms NLR in the SSIM metric. Additionally, all methods demonstrate a reasonable degree of stability for a wide range of values of β.

2) T$_2^*$ map Reconstruction: After the reconstruction of the ten contrast images, the final step is recovering the T_2^* map. For this, we use the 2-parameter model shown in Equation (15) for each pixel of the image. Here, the values of t_i are described in subsection IV-A, and we use the contrasts obtained by the different methods. The metrics are calculated over masked reconstructions that exclude regions of non-physical T_2^* values

(pixels with or adjacent to values of 170 ms or more) to ensure a more meaningful comparison.

Figure 7 and Figure 8 show the reconstructed T_2^* maps for all the methods, at the slices 50 and 70 correspondingly (of the 5th patient), with undersampling factors of $R = 4$, $R = 5$, and $R = 6$. Table II presents the statistical results for the three undersampling factors across 50 slices from the test set.

In the experiments, CConnect consistently outperforms the DeAli and the classic methods in all metrics. Furthermore, both CConnect and DeAli demonstrated superior capability in eliminating aliasing artifacts compared to conventional methods. However, DeAli seems to remove some image details.

V. DISCUSSION

We introduced a novel iterative reconstruction for multi-contrast MRI reconstruction, utilizing trained CNNs in the penalty term. CConnect showed superior performance compared to classical multi-contrast reconstruction methods and a deep learning approach, in terms of visual image quality and PSNR and SSIM metrics. Notably, as the undersampling
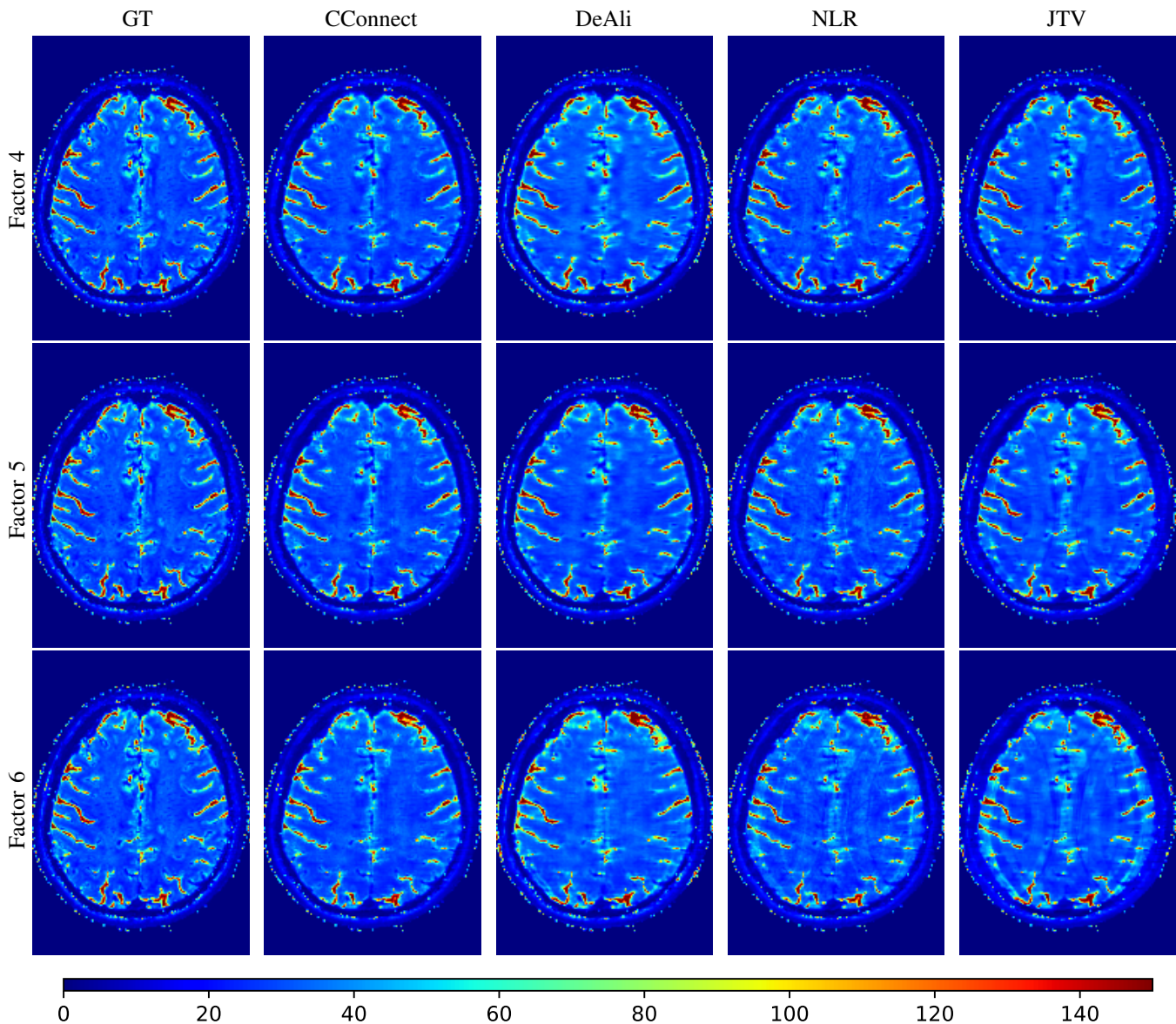
Fig. 7: T_2^* maps for the slice 50 for the GT and different reconstructions methods CConnect, DeAli, NLR and JTV for undersampling factors of $R = 4$, $R = 5$ and $R = 6$.

factor increases, our method outperforms the other methods more noticeably. The CConnect architecture employed in our trained functions, when trained appropriately, is able to remove aliasing artifacts induced by Cartesian undersampling. The utilization of a latent image, playing the role of a mean across contrasts, proved to be crucial as it encapsulates information from all contrasts and undersampling patterns.

The mappings $\{f_i\}$ demonstrated their efficacy by (i) sharing redundant information among contrasts and (ii) effectively eliminating aliasing resulting from undersampling measurements. However, these CNNs are designed for specific undersampling patterns and fixed echo times; therefore, measurements with different trajectories and mapping sequences will require retraining of the proposed CConnect method.

We must point out that the trained $\{f_i\}$ CNNs can be enhanced. For instance, we could potentially improve the model by jointly training the $\{f_i\}$ as a single CNN with n_t

outputs. This architecture could incorporate additional physical aspects of the reconstruction process, such as echo times or direct input of K-space measurements. Additionally, other improvements can be obtained as proposed in [22], [55], [56], where iterative DL models remove artifacts and noise progressively through multiple layered evaluations.

Further improvements in the results could be achieved by fine-tuning all hyperparameters, which was not the primary objective of this paper. Also, weights in the regularizing term, corresponding to a confidence estimation of the trained function $\{f_i\}$, might improve the method, since empirical evidence indicates that all functions do not exhibit similar behavior. Notably, the f_i functions corresponding to intermediate contrasts performs better than functions corresponding to the initial and final contrasts. This observation aligns with our expectations, considering that the mean of the contrasts is more closely related to the central contrasts.
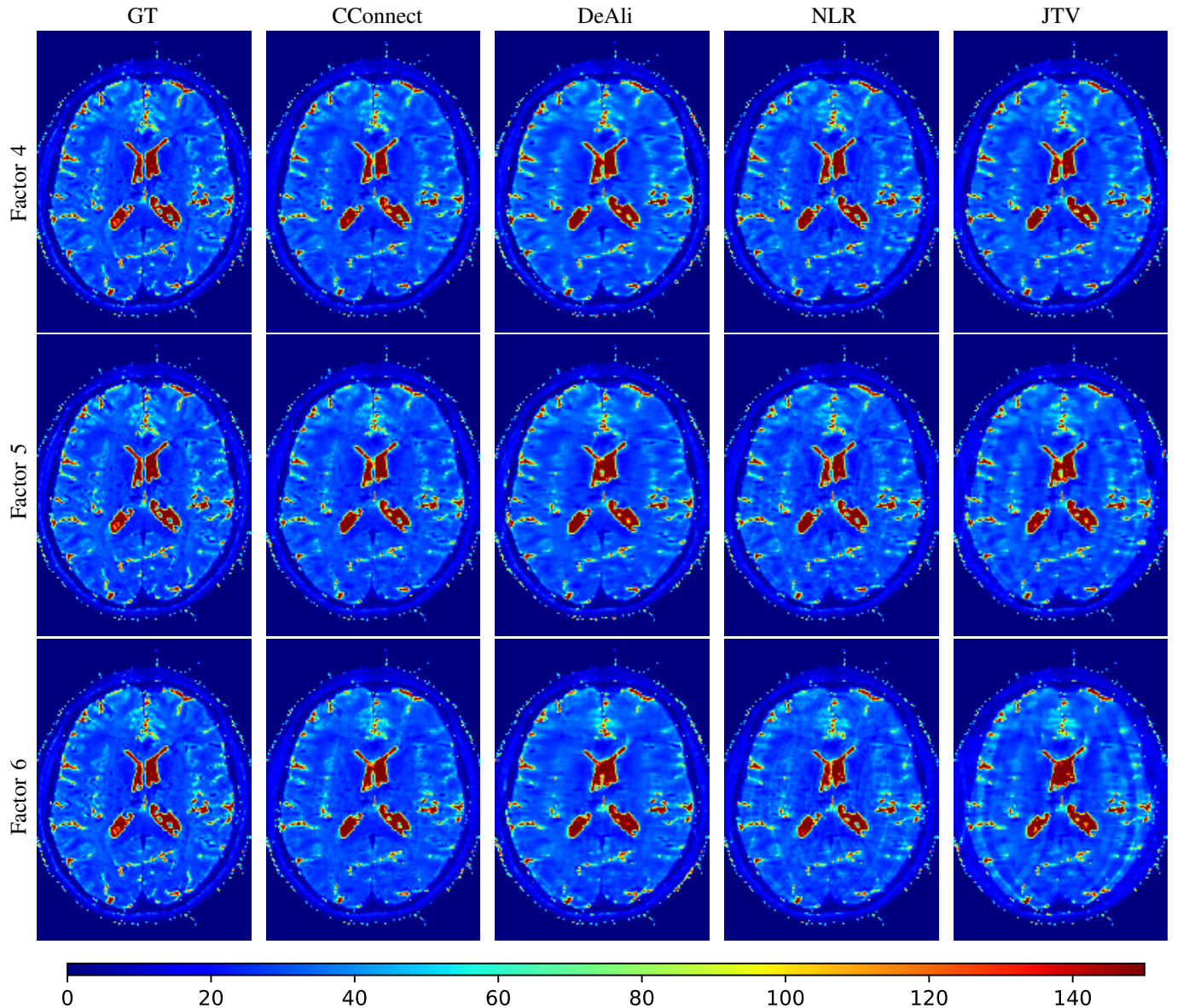
Fig. 8: T_2^* map for the slice 70 for the GT and reconstructions methods CConnect, DeAli, NLR and JTV for undersampling factors of $R = 4$, $R = 5$ and $R = 6$.

A general comment is that improvement in the reconstruction of the contrast images does not automatically translate into an improved reconstruction of the T_2^* maps. Indeed, a large improvement in the reconstruction of the contrast images can become a negligible improvement in the reconstruction of the T_2^* map. This is exemplified in our experiments in the case of sampling factor $R = 4$, where CConnect outperforms JTV in contrast reconstruction (see Table I) but has similar metrics in T_2^* map reconstruction (see Table II). Also, it is important to point out that even if CConnect outperforms the other methods as we increase the subsampling factor R, there is a limit on how much we can undersample and still obtain clinically meaningful T_2^* map reconstructions. The two aspects just mentioned above are inherent challenges of this technique.

In addition, it would be of interest to compare the reconstruction obtained with the proposed CConnect method to reconstruction obtained with other classic methods, such

as WR or switching from the ℓ_1-norm to the ℓ_0 semi-norm. Likewise, the comparisons could encompass other ML techniques, although this presents several challenges as mentioned in Section III-C.

Our study presents several limitations. CConnect was evaluated with retrospective undersampling simulated from magnitude contrast-weighted images, considering a single coil-acquisition. Future work should extend the proposed approach to multi-coil complex value reconstruction from prospectively undersampled k-space data. Furthermore, the proposed approach was tested on data from a single subject. Further testing in a larger cohort of healthy subjects and patients should be investigated as future work. Despite data being 3D, reconstruction was performed in 2D due the limited number of datasets available for training. Extending the proposed reconstruction to 3D will be also of interest. Additionally, the proposed approach was evaluated for T_2^* mapping, however

the framework should be easily extended to other parametric maps and will be investigated in the future.

VI. CONCLUSION

In this study, we developed a synergistic regularization term leveraging trained CNNs. Drawing inspiration from the dictionary method [63] and the methodology presented in [37] for reconstructing CT images across multiple energies, our approach demonstrated notable improvements in T_2^* map reconstructions of the brain compared to state-of-the-art methods. This methodology may be extended to other qMRI parameters as future work. While there are wide options for improvement, our approach may mark a significant step forward in utilizing DL for multicontrast reconstruction.

ACKNOWLEDGMENTS

REFERENCES

[1] J. P. Ridgway, "Cardiovascular magnetic resonance physics for clinicians: part i," *Journal of cardiovascular magnetic resonance*, vol. 12, no. 1, pp. 1–28, 2010.

[2] K. M. Schmainda, "Quantitative imaging in magnetic resonance imaging," in *Quantitative Imaging in Medicine: Applications and Clinical Translation*, pp. 1–1, AIP Publishing LLC Melville, New York, 2021.

[3] V. Gulani and N. Seiberlich, "Quantitative MRI: Rationale and challenges," in *Advances in magnetic resonance technology and applications*, vol. 1, pp. xxxvii–li, Elsevier, 2020.

[4] H. Vrenken, J. J. Geurts, D. L. Knol, L. N. Van Dijk, V. Dattola, B. Jasperse, R. A. Van Schijndel, C. H. Polman, J. A. Castelijns, F. Barkhof, *et al.*, "Whole-brain t1 mapping in multiple sclerosis: global changes of normal-appearing gray and white matter," *Radiology*, vol. 240, no. 3, pp. 811–820, 2006.

[5] A. Müller, A. Jurcoane, S. Kebir, P. Ditter, F. Schrader, U. Herrlinger, T. Tzaridis, B. Mädler, H. H. Schild, M. Glas, *et al.*, "Quantitative t1-mapping detects cloudy-enhancing tumor compartments predicting outcome of patients with glioblastoma," *Cancer medicine*, vol. 6, no. 1, pp. 89–99, 2017.

[6] F. Rugg-Gunn, P. Boulby, M. Symms, G. Barker, and J. Duncan, "Whole-brain t2 mapping demonstrates occult abnormalities in focal epilepsy," *Neurology*, vol. 64, no. 2, pp. 318–325, 2005.

[7] M. J. Knight, B. McCann, D. Tsivos, S. Dillon, E. Coulthard, and R. A. Kauppinen, "Quantitative t2 mapping of white matter: applications for ageing and cognitive decline," *Physics in Medicine & Biology*, vol. 61, no. 15, p. 5587, 2016.

[8] L. Z. Diaz-de Grenu, J. Acosta-Cabronero, J. M. Pereira, G. Pengas, G. B. Williams, and P. J. Nestor, "MRI detection of tissue pathology beyond atrophy in alzheimer's disease: introducing T2-VBM," *Neuroimage*, vol. 56, no. 4, pp. 1946–1953, 2011.

[9] K. Ghassaban, S. Liu, C. Jiang, and E. M. Haacke, "Quantifying iron content in magnetic resonance imaging," *Neuroimage*, vol. 187, pp. 77–92, 2019.

[10] B. L. McGarry, H. J. Rogers, M. J. Knight, K. T. Jokivarsi, A. Sierra, O. H. Gröhn, and R. A. Kauppinen, "Stroke onset time estimation from multispectral quantitative magnetic resonance imaging in a rat model of focal permanent cerebral ischemia," *International Journal of Stroke*, vol. 11, no. 6, pp. 677–682, 2016.

[11] J. Hamilton, D. Franson, and N. Seiberlich, "Recent advances in parallel imaging for MRI," *Progress in nuclear magnetic resonance spectroscopy*, vol. 101, pp. 71–95, 2017.

[12] S. Abu-Hussein, T. Tirer, S. Y. Chun, Y. C. Eldar, and R. Giryes, "Image restoration by deep projected GSURE," in *Proceedings of the IEEE/CVF Winter Conference on Applications of Computer Vision*, pp. 3602–3611, 2022.

[13] J. A. Fessler, "Model-based image reconstruction for MRI," *IEEE signal processing magazine*, vol. 27, no. 4, pp. 81–89, 2010.

[14] A. Majumdar and R. K. Ward, *MRI: Physics, Image Reconstruction, and Analysis*. CRC Press, 2018.

[15] J. C. Ye, "Compressed sensing MRI: a review from signal processing perspective," *BMC Biomedical Engineering*, vol. 1, no. 1, pp. 1–17, 2019.

[16] K. T. Block, M. Uecker, and J. Frahm, "Undersampled radial MRI with multiple coils. iterative image reconstruction using a total variation constraint," *Magnetic Resonance in Medicine: An Official Journal of the International Society for Magnetic Resonance in Medicine*, vol. 57, no. 6, pp. 1086–1098, 2007.

[17] M. Lustig, D. Donoho, and J. M. Pauly, "Sparse MRI: The application of compressed sensing for rapid MR imaging," *Magnetic Resonance in Medicine: An Official Journal of the International Society for Magnetic Resonance in Medicine*, vol. 58, no. 6, pp. 1182–1195, 2007.

[18] M. Lustig, D. L. Donoho, J. M. Santos, and J. M. Pauly, "Compressed sensing MRI," *IEEE signal processing magazine*, vol. 25, no. 2, pp. 72–82, 2008.

[19] M. J. Ehrhardt and M. M. Betcke, "Multicontrast MRI reconstruction with structure-guided total variation," *SIAM Journal on Imaging Sciences*, vol. 9, no. 3, pp. 1084–1106, 2016.

[20] M. Blumenthal, G. Luo, M. Schilling, H. C. M. Holme, and M. Uecker, "Deep, deep learning with BART," *Magnetic Resonance in Medicine*, vol. 89, no. 2, pp. 678–693, 2023.

[21] J. Wang, Q. Yang, Q. Yang, L. Xu, C. Cai, and S. Cai, "Joint optimization of cartesian sampling patterns and reconstruction for single-contrast and multi-contrast fast magnetic resonance imaging," *Computer Methods and Programs in Biomedicine*, vol. 226, p. 107150, 2022.

[22] H. K. Aggarwal, M. P. Mani, and M. Jacob, "MoDL: Model-based deep learning architecture for inverse problems," *IEEE transactions on medical imaging*, vol. 38, no. 2, pp. 394–405, 2018.

[23] S. R. Arridge, P. Maass, O. Öktem, and C.-B. Schönlieb, "Solving inverse problems using data-driven models," *Acta Numerica*, vol. 28, pp. 1–174, 2019.

[24] M. Duff, N. D. Campbell, and M. J. Ehrhardt, "Regularising inverse problems with generative machine learning models," *arXiv preprint arXiv:2107.11191*, 2021.

[25] J. Caballero, A. N. Price, D. Rueckert, and J. V. Hajnal, "Dictionary learning and time sparsity for dynamic MR data reconstruction," *IEEE transactions on medical imaging*, vol. 33, no. 4, pp. 979–994, 2014.

[26] S. Ravishankar and Y. Bresler, "MR image reconstruction from highly undersampled k-space data by dictionary learning," *IEEE transactions on medical imaging*, vol. 30, no. 5, pp. 1028–1041, 2010.

[27] Q. Xu, H. Yu, X. Mou, L. Zhang, J. Hsieh, and G. Wang, "Low-dose x-ray CT reconstruction via dictionary learning," *IEEE transactions on medical imaging*, vol. 31, no. 9, pp. 1682–1697, 2012.

[28] A. Bousse, V. S. S. Kandarpa, K. Shi, K. Gong, J. S. Lee, C. Liu, and D. Visvikis, "A review on low-dose emission tomography post-reconstruction denoising with neural network approaches," *IEEE Transactions on Radiation and Plasma Medical Sciences*, 2024.

[29] A. J. Reader, G. Corda, A. Mehranian, C. da Costa-Luis, S. Ellis, and J. A. Schnabel, "Deep learning for PET image reconstruction," *IEEE Transactions on Radiation and Plasma Medical Sciences*, vol. 5, no. 1, pp. 1–25, 2020.

[30] G. Wang, J. C. Ye, and B. De Man, "Deep learning for tomographic image reconstruction," *Nature Machine Intelligence*, vol. 2, no. 12, pp. 737–748, 2020.

[31] V. Monga, Y. Li, and Y. C. Eldar, "Algorithm unrolling: Interpretable, efficient deep learning for signal and image processing," *IEEE Signal Processing Magazine*, vol. 38, no. 2, pp. 18–44, 2021.

[32] Y. Li, K. Li, C. Zhang, J. Montoya, and G.-H. Chen, "Learning to reconstruct computed tomography images directly from sinogram data under a variety of data acquisition conditions," *IEEE transactions on medical imaging*, vol. 38, no. 10, pp. 2469–2481, 2019.

[33] B. Zhu, J. Z. Liu, S. F. Cauley, B. R. Rosen, and M. S. Rosen, "Image reconstruction by domain-transform manifold learning," *Nature*, vol. 555, no. 7697, pp. 487–492, 2018.

[34] S. Biswas, H. K. Aggarwal, and M. Jacob, "Dynamic MRI using model-based deep learning and SToRM priors: MoDL-SToRM," *Magnetic resonance in medicine*, vol. 82, no. 1, pp. 485–494, 2019.

[35] S. Wang, Z. Su, L. Ying, X. Peng, S. Zhu, F. Liang, D. Feng, and D. Liang, "Accelerating magnetic resonance imaging via deep learning," in *2016 IEEE 13th international symposium on biomedical imaging (ISBI)*, pp. 514–517, IEEE, 2016.

[36] N. J. Pinton, A. Bousse, C. Cheze-Le-Rest, and D. Visvikis, "Multi-branch generative models for multichannel imaging with an application to PET/CT joint reconstruction," *arXiv preprint arXiv:2404.08748*, 2024.

[37] Z. Wang, A. Bousse, F. Vermet, J. Froment, B. Vedel, A. Perelli, J.-P. Tasu, and D. Visvikis, "Uconnect: Synergistic spectral CT reconstruction with U-Nets connecting the energy bins," *IEEE Transactions on Radiation and Plasma Medical Sciences*, 2023.

[38] X. Wang, Z. Tan, N. Scholand, V. Roeloffs, and M. Uecker, "Physics-based reconstruction methods for magnetic resonance imaging," *Philosophical Transactions of the Royal Society A*, vol. 379, no. 2200, p. 20200196, 2021.

[39] S. Bidhult, G. Kantasis, A. H. Aletras, H. Arheden, E. Heiberg, and E. Hedström, "Validation of T1 and T2 algorithms for quantitative MRI: performance by a vendor-independent software," *BMC Medical Imaging*, vol. 16, pp. 1–8, 2016.

[40] P. Blomgren and T. F. Chan, "Color TV: total variation methods for restoration of vector-valued images," *IEEE transactions on image processing*, vol. 7, no. 3, pp. 304–309, 1998.

[41] S. Lefkimmiatis, A. Roussos, M. Unser, and P. Maragos, "Convex generalizations of total variation based on the structure tensor with applications to inverse problems," in *Scale Space and Variational Methods in Computer Vision: 4th International Conference, SSVM 2013, Schloss Seggau, Leibnitz, Austria, June 2-6, 2013. Proceedings 4*, pp. 48–60, Springer, 2013.

[42] M. Guerquin-Kern, D. Van De Ville, C. Vonesch, J.-C. Baritaux, K. P. Pruessmann, and M. Unser, "Wavelet-regularized reconstruction for rapid MRI," in *2009 IEEE International Symposium on biomedical imaging: from nano to macro*, pp. 193–196, IEEE, 2009.

[43] P. Song, L. Weizman, J. F. Mota, Y. C. Eldar, and M. R. Rodrigues, "Coupled dictionary learning for multi-contrast MRI reconstruction," *IEEE transactions on medical imaging*, vol. 39, no. 3, pp. 621–633, 2019.

[44] S. Pandey, A. D. Snider, W. A. Moreno, H. Ravi, A. Bilgin, and N. Raghunand, "Joint total variation-based reconstruction of multiparametric magnetic resonance images for mapping tissue types," *NMR in Biomedicine*, vol. 34, no. 12, p. e4597, 2021.

[45] F. Knoll, K. Bredies, T. Pock, and R. Stollberger, "Total generalized variation (TGV) for MRI," in *Joint Annual Meeting of the International Society of Magentic Resonance in Medicine and the European Society of Magnetic Resonance in Medicine and Biology*, pp. 4855–4855, ., 2010.

[46] M. J. Ehrhardt, K. Thielemans, L. Pizarro, D. Atkinson, S. Ourselin, B. F. Hutton, and S. R. Arridge, "Joint reconstruction of PET-MRI by exploiting structural similarity," *Inverse Problems*, vol. 31, no. 1, p. 015001, 2014.

[47] X. Zhang, D. Guo, Y. Huang, Y. Chen, L. Wang, F. Huang, Q. Xu, and X. Qu, "Image reconstruction with low-rankness and self-consistency of k-space data in parallel MRI," *Medical Image Analysis*, vol. 63, p. 101687, 2020.

[48] A. Perelli, S. A. Garcia, A. Bousse, J.-P. Tasu, N. Efthimiadis, and D. Visvikis, "Multi-channel convolutional analysis operator learning for dual-energy CT reconstruction," *Physics in Medicine & Biology*, vol. 67, no. 6, p. 065001, 2022.

[49] R. S. Stanković and B. J. Falkowski, "The haar wavelet transform: its status and achievements," *Computers & Electrical Engineering*, vol. 29, no. 1, pp. 25–44, 2003.

[50] O. Ronneberger, P. Fischer, and T. Brox, "U-net: Convolutional networks for biomedical image segmentation," 2015.

[51] I. Loshchilov and F. Hutter, "Decoupled weight decay regularization," 2019.

[52] J. R. Shewchuk *et al.*, "An introduction to the conjugate gradient method without the agonizing pain," 1994.

[53] S. Boyd, N. Parikh, E. Chu, B. Peleato, J. Eckstein, *et al.*, "Distributed optimization and statistical learning via the alternating direction method of multipliers," *Foundations and Trends® in Machine learning*, vol. 3, no. 1, pp. 1–122, 2011.

[54] E. Ahishakiye, M. Bastiaan Van Gijzen, J. Tumwiine, R. Wario, and J. Obungoloch, "A survey on deep learning in medical image reconstruction," *Intelligent Medicine*, vol. 1, no. 03, pp. 118–127, 2021.

[55] K. Hammernik, T. Klatzer, E. Kobler, M. P. Recht, D. K. Sodickson, T. Pock, and F. Knoll, "Learning a variational network for reconstruction of accelerated MRI data," *Magnetic resonance in medicine*, vol. 79, no. 6, pp. 3055–3071, 2018.

[56] Y. Liu, Q. Liu, M. Zhang, Q. Yang, S. Wang, and D. Liang, "IFR-net: Iterative feature refinement network for compressed sensing MRI," *IEEE Transactions on Computational Imaging*, vol. 6, pp. 434–446, 2019.

[57] F. Liu, L. Feng, and R. Kijowski, "Mantis: model-augmented neural network with incoherent k-space sampling for efficient mr parameter mapping," *Magnetic resonance in medicine*, vol. 82, no. 1, pp. 174–188, 2019.

[58] J. Mohan, V. Krishnaveni, and Y. Guo, "A survey on the magnetic resonance image denoising methods," *Biomedical signal processing and control*, vol. 9, pp. 56–69, 2014.

[59] A. Haeger, J.-F. Mangin, A. Vignaud, C. Poupon, A. Grigis, F. Boumezbeur, V. Frouin, J.-R. Deverre, M. Sarazin, L. Hertz-Pannier, *et al.*, "Imaging the aging brain: study design and baseline findings of the SENIOR cohort," *Alzheimer's Research & Therapy*, vol. 12, pp. 1–15, 2020.

[60] D. J. Larkman and R. G. Nunes, "Parallel magnetic resonance imaging," *Physics in Medicine & Biology*, vol. 52, no. 7, p. R15, 2007.

[61] J. Bradbury, R. Frostig, P. Hawkins, M. J. Johnson, C. Leary, D. Maclaurin, G. Necula, A. Paszke, J. VanderPlas, S. Wanderman-Milne, and Q. Zhang, "JAX: composable transformations of Python+NumPy programs," 2018.

[62] K.-H. Thung and P. Raveendran, "A survey of image quality measures," in *2009 international conference for technical postgraduates (TECH-POS)*, pp. 1–4, IEEE, 2009.

[63] D. Du, Z. Pan, P. Zhang, Y. Li, and W. Ku, "Compressive sensing image recovery using dictionary learning and shape-adaptive DCT thresholding," *Magnetic resonance imaging*, vol. 55, pp. 60–71, 2019.